

# Evaluating the nature and extent of changes to climate sensitivity between FGOALS-g2 and FGOALS-g3

He Wang <sup>1,2</sup>, Lijuan Li <sup>1</sup>, Xiaolong Chen <sup>1</sup>, Bin Wang <sup>1</sup>

<sup>1</sup> State Key Laboratory of Numerical Modeling for Atmospheric Sciences and Geophysical Fluid Dynamics (LASG), Institute of Atmospheric Physics (IAP), Chinese Academy of Sciences, Beijing, China

<sup>2</sup> College of Earth Sciences, University of Chinese Academy of Sciences, Beijing, China

Corresponding author: Lijuan Li (ljli@mail.iap.ac.cn)

## Key Points:

- Three methods of different complexities for calculating cloud feedbacks are compared.
- The equilibrium climate sensitivity of FGOALS-g3 is smaller than that of FGOALS-g2.
- The equilibrium climate sensitivity decrease in FGOALS-g3 can be attributed mainly to its more cloud and weaker surface albedo feedback.

## Abstract

Equilibrium climate sensitivity (ECS) and its related feedbacks are important metrics used to measure the global mean surface temperature change in future climate projections. This paper uses the radiative kernel approach and a simplified cloud feedback calculation (comparing three different cloud feedback methods) to analyze the differences in the ECS, as well as the feedbacks contributing to it, between two versions of the Flexible Global Ocean-Atmosphere-Land System model (i.e., FGOALS-g2 and FGOALS-g3). The results show that the ECS of FGOALS-g3 is smaller than that of FGOALS-g2 (2.8 K versus 3.3 K). The main feedbacks contributing to the ECS change in FGOALS-g3 are the weaker surface albedo feedback and stronger negative shortwave cloud feedback. The reduced surface albedo feedback in FGOALS-g3 is associated mainly with its mean base state, which has a lower surface air temperature and larger sea ice area compared with FGOALS-g2. The enhanced negative shortwave cloud feedback in FGOALS-g3 is caused mainly by the larger low-cloud area fraction and liquid water path. Furthermore, the ECS change can be traced back to the different cloud parameterization scheme, parameter tuning, ocean grid, and external forcings used in FGOALS-g3, as these all affect the mean climate state of the model.

## Plain Language Summary

Equilibrium climate sensitivity (ECS) is an important quantity as it measures the magnitude of projected warming. However, there is some uncertainty regarding ECS-related feedbacks due to the different methods used to calculate them. Three methods of different complexity used to calculate cloud feedbacks are compared here, and the simplest method is selected to analyze the change in ECS between two versions of the Flexible Global Ocean-Atmosphere-Land System model (i.e., FGOALS-g2 and FGOALS-g3). The main causes of the ECS difference between FGOALS-g3 and FGOALS-g2 are the surface albedo feedback and the shortwave cloud feedback. These are related to the different base states which are further due to the different cloud schemes, parameter tuning, and ocean grids used in the two models. Regional characteristics cause the differences between the surface albedo feedback of the two versions of the model to change over time.

## 1 Introduction

Climate warming is an important topic related to the future of humankind, and carbon dioxide is one of the main greenhouse gases (GHGs) that causes this warming. Equilibrium climate sensitivity (ECS), defined as the equilibrium change in annual global mean surface temperature following a doubling of the atmospheric CO<sub>2</sub> concentration relative to the pre-industrial level (piControl; Flato et al., 2013), can be used to understand how much the Earth's surface temperature will change in response to a certain CO<sub>2</sub> concentration (Zeebe, 2011). The ECS magnitude could be amplified or damped by many feedbacks—an interaction in which a perturbation in one climate quantity causes a change in another, which in turn leads to an additional change in the first quantity (Cubasch and Cess, 1990; Pachauri et al., 2014). The physical feedbacks affecting the ECS include the temperature feedback ( $\lambda_T$ ), water vapor feedback ( $\lambda_{wv}$ ), surface albedo feedback ( $\lambda_a$ ), and cloud feedbacks ( $\lambda_c$ ; Zhang et al., 1994). The temperature feedback can further be decomposed into the Planck feedback ( $\lambda_{\text{Planck}}$ ) and lapse rate feedback ( $\lambda_{LR}$ ).

The ECS range of climate models participating in the Coupled Model Intercomparison Project phase 3 (CMIP3; Randall et al., 2007) was 2.1–4.4 K, and then 2.1–4.7 K for CMIP5 (Flato et al., 2013), and 1.8–5.6 K for CMIP6 (Zelinka et al., 2020), indicating that the large uncertainty in the ECS has not narrowed with the ongoing model development (Soden and Held, 2006). Although the lower limit of climate sensitivity is well-constrained and already provides useful information for policy makers, the upper limit is more difficult to quantify (Knutti and Hegerl, 2008). The wide ECS range in the CMIP models is caused by many factors: different resolutions and/or grids (McGregor, 2015; Doescher et al., 2002), cross-field correlations (Soden et al., 2008), different climate background states (Friedrich et al., 2016), and uncertainties

regarding the evolution of tropical low cloud (Vial et al., 2017). For example, different cloud parameterizations are always considered to be a major factor affecting the ECS (Zhao et al., 2016), and the greater decrease in low cloud coverage and extra-tropical albedo is the main reason for the higher ECS of the CMIP6 models compared with those in CMIP5 (Zelinka et al., 2020). Furthermore, aerosol–cloud interactions are the primary cause of the different ECS in the two versions of the European Centre Earth model, EC-Earth2 and EC-Earth3 (Wyser et al., 2020). In addition, advances in the methods used to calculate the ECS mean our understanding of climate feedbacks is constantly changing; hence, the calculation method is another important link affecting the values of ECS and climate feedback parameters.

A number of methods have been developed to quantify and compare the ECS and the feedbacks contributing to it associated with different models. Among these methods, the one proposed by Gregory et al. (2004) is the most widely used for calculating the ECS of a General Circulation Model (GCM) in which the climate variables respond to a constant forcing, such as an instantaneous doubling or quadrupling of CO<sub>2</sub>. In this method,

$$N = F - H = F + \lambda_{tot}\Delta T_s \quad (1)$$

where  $N$  is the top of atmosphere (TOA) net radiative flux,  $F$  is the radiative forcing induced by the forcing agent,  $H$  is the radiative response caused by the raised CO<sub>2</sub> concentrations, which offsets  $F$ ,  $\lambda_{tot}$  is the total climate feedback parameter, and  $\Delta T_s$  is the change in the near-surface air temperature (SAT). If  $F = H$ , then  $N$  is equal to zero and the SAT change reaches a new equilibrium state  $\Delta T_{eqm}$  (Shine et al., 2003). In this case, in an experiment of abruptly quadrupled CO<sub>2</sub> concentration (abrupt4×CO<sub>2</sub>) relative to the piControl run, the ECS is taken to be half of  $\Delta T_{eqm}$ .

Based on the partial radiative perturbation method (Wetherald and Manabe, 1988), Soden and Held (2006) proposed a widely used technique that decomposes each feedback into two parts: a “radiative kernel”,  $[\partial(N - F)/\partial X]$ , describing the TOA radiative flux response to an incremental change in a variable  $X$  (surface temperature, atmospheric temperature, water vapor, surface albedo, cloud) that depends on the base state of the model, and the climate response of the variable,  $(dX/dT_s)$ . The two parts are combined to measure the feedback amplitude of a particular variable. The radiative kernel part implies that there is a linear relationship between the TOA radiative flux and the perturbed variable. However, because cloud processes are nonlinear, cloud feedbacks are more appropriately calculated in a different way (Shell et al., 2008).

The simplest method to calculate the cloud feedback parameter is to regress the change in cloud radiative forcing (CRF) onto the change in global average SAT between the doubled- $\text{CO}_2$  run and piControl run (Cess and Potter, 1988). Alternatively, the cloud feedback parameter can be calculated as the residual difference between the total climate feedback ( $\lambda_{tot}$ ) and the sum of the other feedbacks ( $\lambda_T$ ,  $\lambda_\alpha$ , and  $\lambda_{WV}$ ; Soden and Held 2006; Senior and Mitchell, 2000).

To further reduce the sensitivity to uncertainties caused by external radiative forcings, another method has been proposed that involves adjusting the model-simulated change in CRF to account for cloud masking effects (Soden et al., 2008). For example, in the Community Atmosphere Model version 5 (CAM5), the cloud forcing was adjusted to account for the direct and indirect effects of GHGs and aerosols by introducing a “GHG kernel” and “aerosol kernel”, which remove the forcing effects of GHGs and aerosols, respectively (Hansen et al., 2005; Gettelman et al., 2016). In addition, to correct for changes in non-cloud variables that can alter the cloud feedback, Vial et al. (2013) used the difference in the kernels for temperature, water

vapor, and surface albedo between all-sky and clear-sky conditions as part of the cloud feedback term.

Yet another method to determine cloud feedbacks is to use overcast-sky CRF histograms, where “overcast” indicates that cloud covers the entire atmospheric column in the radiation code. In this method, zonal and monthly mean annual cycles of temperature and water vapor profiles are averaged together as input to the Fu and Liou (1992) radiation code (Zelinka et al., 2012).

In brief, although the ECS calculation proposed by Gregory et al. (2004) is the most commonly used, methods of different complexity are used to calculate feedbacks contributing to the ECS, especially the cloud feedback. These methods all produce different feedback parameter values, which makes it difficult to directly compare different studies. Consequently, one aim of this study is to compare the values of the cloud feedback parameter obtained using different methods and to identify the method that results in the smallest residual value. Another aim is to analyze the change in the ECS, as well as the feedbacks contributing to that change, between two versions of the Flexible Global Ocean-Atmosphere-Land System model, FGOALS-g2 and FGOALS-g3, which are participating in CMIP5 and CMIP6, respectively.

The remainder of this paper is organized as follows. The two versions of the FGOALS-g model and the comparison of different cloud feedback methods are described in section 2. The analysis of ECS and the contributing feedback components are presented in section 3. A summary and discussion are provided in section 4.

## **2 Model Description, Methods, and Data Processing**

### **2.1. Model Description**

FGOALS-g is a coupled model developed at the State Key Laboratory of Numerical Modeling for Atmospheric Sciences and Geophysical Fluid Dynamics (LASG), part of the

Institute of Atmospheric Physics (IAP) of the Chinese Academy of Sciences. The model currently has three formal versions; i.e., FGOALS-g1, FGOALS-g2, and FGOALS-g3, which have participated in CMIP3, CMIP5, and CMIP6 respectively (Li et al., 2007, 2013a, 2020a). These versions of FGOALS-g comprise four component models (i.e., the atmospheric model, ocean model, sea ice model, and land surface model) and a coupler. Compared with FGOALS-g2, the components were updated in FGOALS-g3 as follows. The Grid-point Atmospheric Model of LASG/IAP version 3 (GAMIL3; Li et al., 2020b) was used instead of GAMIL2 (Li et al., 2013b), the LASG/IAP Climate system Ocean Model version 3 (LICOM3; Yu et al., 2018) was used in place of LICOM2 (Liu et al., 2012), the Land Surface Model for Chinese Academy of Sciences (CAS-LSM; Xie et al., 2018) was used rather than the Community Land Model version 3 (CLM3, Oleson et al., 2004), the coupler 6 (Craig et al., 2005) was upgraded to the coupler 7 (Craig et al., 2012), and the external forcings recommended by CMIP6 (Eyring et al., 2016) were used instead of those from CMIP5 (Taylor et al., 2012). The upgrades of the component models focus mainly on the horizontal grid resolution, physical processes, and tuning parameters (Li et al., 2020a). In both FGOALS-g2 and FGOALS-g3, the sea ice model is the Community Ice Code version 4 (CICE4). CAS-LSM is based on CLM4.5 (Oleson et al., 2013) and takes into account the effects of lateral groundwater flow (Xie et al., 2012; Zeng et al., 2018), human water intake (Zou et al., 2014; Zeng et al., 2016), soil freezing and thawing interface changes (Gao et al., 2016; 2019), and river nitrogen transport processes (Liu et al., 2019).

## 2.2. Methods



Our feedback calculations were based on the radiative kernels of CAM5 (Pendergrass et al., 2018) and used three different cloud feedback methods. The default method was to use the sum of the net TOA radiation flux change under GHG forcing and aerosol forcing as cloud masking of radiative forcing, which may be written as follows:

$$\lambda_{tot} = \lambda_{sum} + Res = \lambda_T^{whole\ sky} + \lambda_{WV}^{whole\ sky} + \lambda_{\alpha}^{whole\ sky} + \lambda_c + Res \quad (2)$$

$$\lambda_c = \frac{\Delta CRE}{\Delta T_s} + \frac{\Delta CRE^{GHG}}{\Delta T_s} + \frac{\Delta CRE^{Aerosol}}{\Delta T_s} + \sum_x (\lambda_x^{clear\ sky} - \lambda_x^{whole\ sky}) \quad (3)$$

The left-hand side of Eq. (2) is the total feedback ( $\lambda_{tot}$ ) corresponding to the ECS calculated by the Gregory et al. (2004) method. The first term on the right-hand side of Eq. (2) is the sum of all feedback components ( $\lambda_{sum}$ ) calculated using the radiative kernels of CAM5, which include the temperature feedback ( $\lambda_T^{whole\ sky}$ ), the water vapor feedback ( $\lambda_{WV}^{whole\ sky}$ ), and the surface albedo feedback ( $\lambda_{\alpha}^{whole\ sky}$ ) of the whole sky, as well as the cloud feedback ( $\lambda_c$ ). The second term on the right-hand side is a residual term ( $Res$ ). In Eq. (3),  $\Delta CRE$  is the change in cloud radiative effect (CRE), in which the CRE is the difference between the TOA whole-sky radiative flux and clear-sky radiative flux. The second and third terms on the right-hand side of Eq. (3) are the GHG forcing and aerosol forcing adjustment terms, respectively. The fourth term on the right-hand side of Eq. (3),  $[\sum_x (\lambda_x^{clear\ sky} - \lambda_x^{whole\ sky})]$ , is the sum of differences between whole-sky and clear-sky feedbacks (except for the cloud feedback).

Another relatively simple cloud feedback method used in this study is that of Soden et al. (2004):

$$\lambda_c = \frac{\Delta CRE}{\Delta T_s} + \lambda_{cloud\ corr} \quad (4)$$

$$\lambda_{cloud\ corr} = \sum_x (\lambda_x^{clear\ sky} - \lambda_x^{whole\ sky}) \quad (5)$$

Eq. (4) is relatively accurate when perturbations are small, however its accuracy decreases when perturbations become large, as in the abrupt4×CO<sub>2</sub> experiments (Jonko et al., 2012; Block and Mauritsen, 2013). Eq. (4) can alternatively be written as:

$$\lambda_c = \frac{\Delta CRE}{\Delta T_s} + (\lambda_T^{clear\ sky} - \lambda_T^{whole\ sky} + \lambda_{WV}^{clear\ sky} - \lambda_{WV}^{whole\ sky} + \lambda_\alpha^{clear\ sky} - \lambda_\alpha^{whole\ sky}) \quad (6)$$

Combining Eq. (2) and Eq. (6),

$$\lambda_{tot} = \lambda_T^{clear\ sky} + \lambda_{WV}^{clear\ sky} + \lambda_\alpha^{clear\ sky} + \frac{\Delta CRE}{\Delta T_s} + Res \quad (7)$$

The methods that are based on Eq. (3) and Eq. (4) require the use of kernel data to calculate the cloud feedback, but the following method does not. In this method, the cloud feedback term (Chen et al., 2014) is simplified as:

$$\lambda_c = \frac{\Delta CRE}{\Delta T_s} \quad (8)$$

Using Eq. (8) to replace the cloud feedback term in Eq. (2):

$$\lambda_{tot} = \lambda_T^{whole\ sky} + \lambda_{WV}^{whole\ sky} + \lambda_\alpha^{whole\ sky} + \frac{\Delta CRE}{\Delta T_s} + Res \quad (9)$$

If the second and third terms on the right-hand side of Eq. (3),  $\frac{\Delta CRE^{GHG}}{\Delta T_s}$  and  $\frac{\Delta CRE^{Aerosol}}{\Delta T_s}$ , are zero, then Eq. (2) becomes equivalent to Eq. (7). If the second term on the right-hand side of Eq. (4),  $\lambda_{cloud\ corr}$ , is zero, then Eq. (7) becomes equivalent to Eq. (9).

In real calculations, there are large uncertainties associated with the residual term among different kernel methods (Vial et al., 2013). Therefore, we compared the residuals calculated using three different methods: the CAM5 radiative kernel method (Eq. (2) and Eq. (3), group 1), the wholly simplified method (Eq. (9), group 2), and the simplified method (Eq. (7), group 3; Fig. 1). In the three methods, except for the calculation of cloud feedback is different, the calculation of other feedback is identical, different cloud feedback methods have great influence

(about 0.3~0.7) on the cloud feedback and final residual in multi-model comparison. The residual amplitude in group 2 ( $\lambda_{cloud\_corr} = 0$ ) was the smallest among the three groups in both versions of FGOALS-g. It should be noted that in group 1, the GHG and aerosol forcing experiments of CAM5 were used to calculate the FGOALS-g feedback. As these experiments were not performed using FGOALS-g, this may be one of the reasons for the large residual associated with this method. We used the wholly simplified method based on Eq. (9) in the following analysis because of its simple calculation, easy operation, clear physical meaning, and small residual.

To further investigate the source of the residual term, we divided the residual in Eq. (9) into longwave (LW) and shortwave (SW) components as follows. Eq. (9) can be rewritten as:

$$\lambda_T + \lambda_{WV} + \lambda_\alpha + \lambda_c + Res = \frac{R_{SW} - R_{LW}}{\Delta T_s} \quad (10)$$

where the net radiative flux ( $R$ ) is set to be positive downward and negative upward. The feedbacks calculated by kernels were separated into LW and SW radiative fluxes ( $R_{LW}$  and  $R_{SW}$ ). The LW and SW radiative feedbacks are written as:

$$\lambda_T + \lambda_{LW_{WV}} + \lambda_{LW_c} + Res_{LW} = \frac{-R_{LW}}{\Delta T_s} = \lambda_{LW} \quad (11)$$

$$\lambda_\alpha + \lambda_{SW_{WV}} + \lambda_{SW_c} + Res_{SW} = \frac{R_{SW}}{\Delta T_s} = \lambda_{SW} \quad (12)$$

where  $Res_{LW}$  and  $Res_{SW}$  are the residuals of the difference between the total feedback and the sum of the LW and SW component feedbacks, respectively.

### 2.3. Data Processing

During post-processing of the model data, the stratosphere is masked, with the height of the tropopause crudely estimated at 100 hPa in the tropics and lowered to 300 hPa at the poles. As

introduced in Soden and Held (2006), we use decadal means to compare FGOALS-g3 with FGOALS-g2 to diminish interannual variability. Considering the dependence of ECS on data length (Senior and Mitchell, 2000), the 150-year abrupt4×CO<sub>2</sub> and piControl simulations were divided into fast-response (years 1–20) and slow-response (years 21–150) stages to facilitate a more comprehensive understanding of the differences between the two model versions. In addition, there is an assumption that the radiative flux of a variable X is calculated independently for each layer, which is generally valid at the global scale (Colman and McAvaney, 1997).

### 3 Results

#### 3.1. Equilibrium Climate Sensitivities and Feedbacks

The ECS was 2.8K for FGOALS-g3 and 3.3K for FGOALS-g2 when using the 150-year dataset, but this increased to 3.0K and 3.7K for FGOALS-g3 and FGOALS-g2, respectively, when considering only the slow-response stage (years 21–150; Fig. 2). Thus, there was a 0.2K and 0.4K difference in the ECS of FGOALS-g3 and FGOALS-g2, respectively, when considering only later years in the simulation, which we attribute to their different fast- and slow-response stages.

The SAT anomaly (SATA) variation in the 150<sup>th</sup> year of the FGOALS-g3 simulation was smaller than that of FGOALS-g2 (Fig. 3a, solid line), which is consistent with the change in the ECS. However, the changes of the SATA were significantly different in the fast- and slow-response stages between the two model versions; compared with FGOALS-g2, changes were larger in the fast-response stage and smaller in the slow-response stage in FGOALS-g3. As with the global mean SATA evolution, the decrease of the sea ice area (SIA) in the Northern Hemisphere occurred faster (slower) in FGOALS-g3 in the fast- (slow-) response stage than in

FGOALS-g2 (Fig. 3b, solid line). The decrease of the SIA in the Southern Hemisphere was consistently slower in FGOALS-g3 than in FGOALS-g2 throughout the whole simulation. In addition, the global mean SAT of FGOALS-g3 was higher by about 0.75K than that of FGOALS-g2 in the piControl simulation (Fig. 3a, dashed line), whereas the SIA in the Northern Hemisphere of FGOALS-g3 was larger than that of FGOALS-g2 (Fig. 3b, dots). Overall, the different evolution of the SAT in the fast- and slow-response stages between the two model versions was associated with the sea ice reduction.

During the slow-response stage, the value of  $\lambda_{\text{sum}}$  was relatively close to  $\lambda_{\text{tot}}$ , again demonstrating the small residual of our chosen feedback calculation method (Fig. 4). The difference in  $\lambda_{\text{tot}}$  between the two model versions can be attributed to the differences in each feedback. How much each feedback contributes depends on the dataset length, because the climate feedback amplitudes are related to the dataset length used (Table 1).

Considering the full dataset length (Fig. 4, triangles), the differences in the lapse rate feedback, water vapor feedback, and surface albedo feedback more or less cancel out, resulting in the cloud feedback contributing the most to the ECS difference. That is, the stronger negative cloud feedback in FGOALS-g3 is the main reason for the ECS decrease from FGOALS-g2 to FGOALS-g3, which is consistent with the result that stronger positive cloud feedbacks contribute to the higher multi-model mean ECS of CMIP6 models compared with CMIP5 models (Zelinka et al., 2020; Table 1).

During the slow-response stage (Fig. 4, hollow circles), the difference in the surface albedo feedback between the two model versions was close to that of the cloud feedback, and was therefore another main contributor to the lower ECS in FGOALS-g3. The causes of these changes will be discussed in sections 3.2 and 3.3.

### 3.2. Surface Albedo Feedback

The surface albedo feedback is closely related to changes in SIA. As described in the previous section, the SIA evolution in both polar regions during the slow-response stage is consistent with the variation in SAT; i.e., the SIA decreases less in FGOALS-g3 than in FGOALS-g2, and the SAT increases less in FGOALS-g3 than in FGOALS-g2. Changes in the surface albedo feedback unfold differently in the three stages considered here, so for simplicity and brevity, in the following we focus on the Arctic region only.

The overall change in the surface albedo feedback between the two model versions arises mainly during the slow-response stage around the center of the Arctic, during the fast-response stage in the Okhotsk Sea, and during both the fast- and slow-response stages in the North Atlantic and Bering Sea (not shown). Figure 5 shows the differences in the surface albedo feedback, SAT, and SIA between the abrupt4×CO<sub>2</sub> and piControl simulations in the center of the Arctic, North Pacific (Bering Sea and Okhotsk Sea), and North Atlantic (Davis Strait, Labrador Sea, and Norway Sea) in the fast- and slow-response stages.

In the fast-response stage, the SIA decrease in FGOALS-g3 occurs significantly faster than in FGOALS-g2 in the North Atlantic, North Pacific, and Hudson Bay, which could be associated with the relatively large SIA at the edge of the Arctic region in FGOALS-g3. Hence the range and amplitude of the warming in FGOALS-g3 are larger than in FGOALS-g2 (Fig. 5a and 5b). In the central Arctic, although the decrease in SIA in FGOALS-g3 occurs slightly slower than in FGOALS-g2, the mean SIA decreases faster in the Northern Hemisphere (Fig. 3b). These results show that the SIA change in the central Arctic does not dominate the stronger surface albedo

feedback in FGOALS-g3 during the fast-response stage, but rather the SIA change at the edge of the Arctic region is dominant (Table 1).

In the Okhotsk Sea and North Atlantic (Davis Strait, Labrador Sea, and Norway Sea), the difference in the surface albedo feedback during the fast-response stage between the two model versions is also related to changes in the ocean circulation. The Atlantic meridional overturning circulation (AMOC) is important in regulating the pace of surface warming (Medhaug and Furevik, 2011; Chen and Tung, 2018). The AMOC index, defined as the maximum of the meridional overturning stream function between 15°N and 65°N below 500 m in depth, decreases significantly faster in FGOALS-g3 (about -21 Sv) than in FGOALS-g2 (about -8 Sv) during the fast-response stage (Fig. 6). The stronger AMOC and AMOC decrease are closely associated with the faster changes in SAT, SIA, and surface albedo feedback in FGOALS-g3.

On the other hand, during the slow-response stage, the AMOC remains essentially unchanged in both model versions, which is similar to the small changes seen during the slow-adjustment stage in the Geophysical Fluid Dynamics Laboratory (GFDL) model (He et al., 2017). During the slow-response stage, the change in SIA in the central Arctic is consistent with the finding that differences in the surface albedo feedback between models stem mainly from the sensitivity of the surface albedo to surface temperature (Winton, 2006). That is, the more regional snow and sea ice there is, the higher the surface albedo, which leads to lower local temperatures, thus promoting the increase of regional snow and sea ice, and vice versa. The positive surface albedo feedback loop in FGOALS-g3 is slower than in FGOALS-g2 during the slow-response stage around the center of the Arctic (Fig. 5c and 5d) and eventually dominates the change in surface albedo feedback in the simulation as a whole, which is closely related to the lower background temperature in FGOALS-g3 (about 2 K lower). Moreover, the weak

AMOC of FGOALS-g3 in the slow stage will weaken the heat northward transport in the upper ocean level, which can contribute to slow down the warming (Fig. 6). Levermann et al. (2007) also pointed out that the positive relationship between mean AMOC and AMOC decline under CO<sub>2</sub> forcing is mediated by sea ice. However, the relationship among AMOC, SAT and SIA is complex in CMIP5 or CMIP6 models which is not simply to promote or inhibit the change of ECS among different models (Weijer et al., 2020).

In general, the difference in the surface albedo feedback between FGOALS-g2 and FGOALS-g3 can be attributed mainly to their different climate base states; i.e., the lower temperature, larger sea ice cover, stronger AMOC in FGOALS-g3 in the piControl simulation, and weaker AMOC in FGOALS-g3 in the slow-response stage. These mean-state differences are further related to the different external forcings used in CMIP5 and CMIP6, and the different ocean grids used in the two model versions; in FGOALS-g3, the ocean grid was updated from a latitude-longitude grid to a tripolar grid (Li et al., 2017; Lin et al., 2020; Li et al., 2020a).

### 3.3. Cloud Feedback

Different types of clouds have different radiative effects (Zelinka et al., 2012). Low clouds reflect solar radiation and therefore have a cooling effect, whereas high clouds absorb the LW radiation emitted by the Earth and so have a warming effect. Consequently, the net effect (cooling or warming) depends on the type of clouds present. In the FGOALS-g model, the CRF calculations are closely associated with the cloud area fraction (CAF) and liquid water path (LWP; Li et al., 2014, 2015). The CAF anomaly increases significantly faster in FGOALS-g3 than in FGOALS-g2 in the simulation as a whole and the difference in the CAF between the two model versions at the 150<sup>th</sup> year reaches about 1.2% (Fig. 7a). Moreover, the piControl CAF of



FGOALS-g3 is higher by about 0.8% than that of FGOALS-g2 (Fig. 7a). The LWP anomaly at the 150<sup>th</sup> year of FGOALS-g3 is also higher by about 1.5 g m<sup>-2</sup> than in FGOALS-g2, and the LWP in the FGOALS-g3 piControl run is higher by about 12 g m<sup>-2</sup> than in FGOALS-g2 (Fig. 7b). However, the ice water path (IWP) anomaly at the 150<sup>th</sup> year of FGOALS-g3 decreases by about 0.4 g m<sup>-2</sup> more than in FGOALS-g2, and the background IWP of FGOALS-g3 is lower by about 2 g m<sup>-2</sup> than in FGOALS-g2 (Fig. 7b). The change in the condensed water path includes changes to the LWP and IWP, and comes mainly from the LWP, as the IWP changes less in the FGOALS-g models. As pointed out in many studies, the changes in LWP affect cloud scattering, which leads to a big difference in the cloud feedback between the two model versions and further affects the ECS (Turner et al., 2007; Zelinka et al., 2012; Bodas-Salcedo et al., 2016).

Compared with FGOALS-g2, FGOALS-g3 has a higher CAF and LWP, and a stronger negative cloud feedback (Table 1). This is consistent with the amplification of the water vapor feedback (Silvers et al., 2018). Figure 8 shows that the difference in the spatial distribution of cloud feedbacks between the two model versions, especially the SW cloud feedback, is more prominent around the equatorial South Pacific and Indian Ocean (the sea area near the Indonesian islands), and the Southern Ocean, whereas the water vapor feedback is clearly enhanced in the equatorial South Pacific in FGOALS-g3. Many observational and model simulation studies have shown that supercooled liquid clouds are ubiquitous over the Southern Ocean and contribute about one-third of the reflected solar radiation during the austral summer (Hu et al., 2010; Huang et al., 2015; Zelinka et al., 2012; Bodas-Salcedo et al., 2016; Bacmeister et al., 2020).

Zelinka et al. (2020) showed that the stronger positive net cloud feedback in CMIP6 arises primarily from the SW low-cloud component, whereas the non-low-cloud feedback has slightly

decreased in the CMIP6 models compared with the CMIP5 models. On average, the SW low-cloud feedback is more positive in CMIP6 due to larger reductions in low-cloud cover and smaller increases in LWP with warming. The change in the SW low-cloud feedback from FGOALS-g2 to FGOALS-g3 is just the opposite of the change in the multi-model mean from CMIP5 to CMIP6. The SW low-cloud feedback in FGOALS-g3 is more negative than that in FGOALS-g2 (Fig. 8c). This stronger negative SW low-cloud feedback can be attributed to the larger CAF and LWP in the piControl run, which enhances cloud scattering and suppresses the temperature increase near the ground.

Low cloud (i.e., below 700 hPa) and high cloud (i.e., above 400 hPa) increase more in response to a quadrupling of CO<sub>2</sub> in FGOALS-g3 than in FGOALS-g2, and vice versa for mid-level cloud (Fig. 9). As in most models, the change in the low-cloud SW feedback dominates the net cloud feedback in FGOALS-g3 (Zelinka et al., 2020). In some of the climate models participating in CMIP3, the low-cloud SW feedback in the equatorial region has an opposite trend to the mid-level-cloud SW feedback (Zelinka et al., 2012), which is consistent with the increase in low clouds and decrease in mid-level clouds in FGOALS-g3. Moreover, the enhancement of the low-cloud SW feedback is related to the thickening of low clouds in FGOALS-g3. The vertical profile of the CAF in Fig. 9 also shows that the cloud cover in both FGOALS-g2 and FGOALS-g3 is basically constant within each layer throughout the simulation. This may be because the low-level CAF and LWP in the piControl simulations differ between the two model versions. The low-level CAF and LWP of the climate base state in FGOALS-g3 are higher than in FGOALS-g2, which is primarily caused by the reduction in the high-cloud relative humidity threshold, the changed stratocumulus cloud scheme, and the parameter tuning

(especially the stability trigger for stratus clouds and relative humidity threshold for layer clouds)  
in FGOALS-g3 (Li et al., 2020b).

## **4 Discussion and Conclusions**

In this study, we compared three methods of differing complexity that can be used to calculate the cloud feedback in two versions of the FGOALS-g coupled climate model and found that, the methods of cloud feedback have great influence (about 0.3~0.7) on cloud feedback in two versions of the FGOALS-g. Moreover, in both FGOALS-g2 and FGOALS-g3, the residual term is smallest when the cloud feedback parameter is simply equal to the change in CRE normalized by the change in surface temperature. Based on this simplified method, we analyzed the differences in the ECS and its related physical feedbacks between the two versions of the model. Applying an abrupt4×CO<sub>2</sub> scenario relative to the piControl run, we obtained ECS values, calculated using a 150-year linear regression (whole-response stage) and a two-stage (fast-response and slow-response stage) linear regression of 2.8K and 3.0K, respectively, from FGOALS-g3, and 3.3K and 3.7K, respectively, from FGOALS-g2.

The main feedbacks contributing to the ECS reduction from FGOALS-g2 to FGOALS-g3 were the surface albedo feedback and cloud feedback, although other feedbacks also have impacts. The negative cloud feedback is strengthened in FGOALS-g3 during the fast, slow, and whole-response stages. The positive surface albedo feedback was weakened in FGOALS-g3 during the slow and whole-response stages, but was still the biggest term during the slow-response stage, whereas it is strengthened during the fast-response stage, which is related to the change in ocean–atmosphere interaction between the fast- and slow-response stages.

430 Compared with FGOALS-g2, during the fast-response stage of FGOALS-g3, the SIA in the  
431 Northern Hemisphere decreased faster, the SAT increased faster, and the surface albedo  
432 feedback became stronger in the abrupt4×CO<sub>2</sub> scenario relative to the piControl run. This  
433 change can be attributed to the SIA at the edge of the Arctic being larger in FGOALS-g3 than in  
434 FGOALS-g2, which causes it to melt more rapidly, and this is the result of the large  
435 change/mean state in the AMOC intensity during the fast-response/piControl stage. During the  
436 slow-response stage, the changes in SIA occur mainly in the center of the Arctic. This can also  
437 be attributed to the larger SIA and lower SAT in the center of the Arctic in FGOALS-g3 than in  
438 FGOALS-g2, which makes it harder for the ice to melt in FGOALS-g3. These features are  
439 related to the different climate background states in the two model versions, which are caused by  
440 the different external forcings recommended by CMIP5 and CMIP6, and the different ocean  
441 grids used (i.e., a latitude-longitude grid is used in FGOALS-g2 and a tripolar grid in FGOALS-  
442 g3; Li et al., 2017; Lin et al., 2020; Li et al., 2020a).

443 The difference in the cloud feedback between the versions of the two model is more  
444 prominent in the equatorial Pacific, Indian Ocean, and Southern Ocean, and this is associated  
445 with the increased low CAF and LWP in the piControl run of FGOALS-g3. Compared with the  
446 multi-model average results of Zelinka et al. (2020), the change in the cloud feedback was also  
447 the main cause of the change in ECS between FGOALS-g2 and FGOALS-g3, but the reasons for  
448 the change in this cloud feedback differ. In particular, the differences in the cloud fraction  
449 scheme and parameter (threshold for cloud formation) tuning between FGOALS-g2 and  
450 FGOALS-g3 are important. In addition, the change in the surface albedo feedback is an  
451 important contributing factor to the change in ECS. Compared with the EC-Earth model results  
452 of Wyser et al. (2020) in which the aerosol-cloud interactions contribute to the change of ECS,

the aerosol-cloud interaction scheme keep the same in two FGOALS-g versions in two simulations (piControl and abrupt4×CO<sub>2</sub>).

In brief, we attribute the changes in the cloud feedback in FGOALS-g3 primarily to the different LWP and CAF in the climate base state, especially regarding low clouds. These changes are associated with the reduction of the high-cloud relative humidity threshold, the different stratocumulus cloud scheme, and different tuning parameters used in FGOALS-g3 (Li et al., 2020a).

Using multi-model statistics, Tian (2015) found that weak (strong) double Intertropical Convergence Zone (ITCZ) biases correspond to high (low) ECS values in CMIP5. However, FGOALS-g2 shows a stronger double ITCZ than FGOALS-g3 (Li et al., 2020a), and yet the ECS in FGOALS-g2 is higher than that in FGOALS-g3. Indeed, the emergent relationship between ECS and a double-ITCZ bias was found to be barely significant in CMIP6 (Schlund et al., 2020). Moreover, the increase in low cloud coverage has a stronger cooling effect in the high latitudes of the Northern Hemisphere (e.g., the North Atlantic) in FGOALS-g3, which slows down the temperature increase in that area and affects the feedback between temperature and surface albedo. In addition, the change in the cloud feedback in the North Atlantic is related to the AMOC; the stronger interaction between the AMOC and cloud feedback in FGOALS-g3 also leads to a stronger negative cloud SW feedback in that area.

The cloud feedback can be divided into LW and SW feedbacks. We calculated and compared the LW and SW feedbacks in the sum of the component results (left side of Eq. (11) and Eq. (12)) and the model net long wave results (right side of Eq. (11) and Eq. (12)). The LW (Fig. 10a and 10b) and SW (Fig. 10c and 10d) residuals in FGOALS-g3 in the equatorial Pacific are significantly greater than in FGOALS-g2, indicating a strong correlation between the cloud

and other feedbacks, especially the water vapor feedback. The LW and SW residuals in FGOALS-g3 at the two poles are slightly less than in FGOALS-g2, indicating a weak relationship between the cloud and other feedbacks. In addition, the uncertainty of cloud feedback comes from the selection of different cloud feedback methods. Some methods calculate negative feedback, while others can calculate positive feedback. No matter how complex they are, their residual terms are difficult to explain clearly. Moreover, the influence of internal variability during the slow-response stage cannot be ignored.

#### **Acknowledgments**

This research was jointly funded by the National Natural Science Foundation of China (Grants 41775101 and 41622503), the Strategic Priority Research Program of Chinese Academy of Sciences (Grant XDB42010404), and the National Key Research Project (Grant 2016YFB0200805). The simulated datasets are available by searching for FGOALS-g2 and/or FGOALS-g3 on the ESGF-node (<https://esgf-node.llnl.gov/projects/cmip5/> and <https://esgf-node.llnl.gov/projects/cmip6/>).

## References

- Bacmeister, J. T., C. Hannay, B. Medeiros, A. Gettelman, R. Neale, H. B. Fredriksen, et al. (2020). CO<sub>2</sub> increase experiments using the Community Earth System Model (CESM): Relationship to climate sensitivity and comparison of CESM1 to CESM2. *Journal of Advances in Modeling Earth Systems*, e2020MS002120. <https://doi.org/10.1029/2020MS002120>
- Block, K., and T. Mauritsen (2013). Forcing and feedback in the MPI-ESM-LR coupled model under abruptly quadrupled CO<sub>2</sub>. *Journal of Advances in Modeling Earth Systems*, 5(4), 676–691. <https://doi.org/10.1002/jame.20041>
- Bodas-Salcedo, A., T. Andrews, A. V. Karmalkar, and M. A. Ringer (2016). Cloud liquid water path and radiative feedbacks over the Southern Ocean. *Geophys. Res. Lett.*, 43, 10,938–10,946. <https://doi.org/10.1002/2016GL070770>
- Cess, R. D., and G. L. Potter (1988). A methodology for understanding and intercomparing atmospheric climate feedback processes in general-circulation models. *Journal of Geophysical Research: Atmospheres*, 93(D7), 8305–8314. <https://doi.org/10.1029/JD093iD07p08305>
- Chen, X. L., T. J. Zhou, and Z. Guo (2014). Climate sensitivities of two versions of FGOALS model to idealized radiative forcing. *Science China Earth Sciences*, 57(6), 1363–1373. <https://doi.org/10.1007/s11430-013-4692-4>
- Chen, X. Y., Tung, K. (2018). Global surface warming enhanced by weak Atlantic overturning circulation. *Nature*, 559, 387–391. <https://doi.org/10.1038/s41586-018-0320-y>
- Colman, R. A., and B. J. McAvaney (1997). A study of general circulation model climate feedbacks determined from perturbed sea surface temperature experiments. *Journal of Geophysical Research: Atmospheres*, 102(D16), 19383–19402. <https://doi.org/10.1029/97jd00206>
- Craig, A. P., Jacob, R., Kauffman, B., Bettge, T., Larson, J., E. Ong, et al. (2005). CPL6: The new extensible, high performance parallel coupler for the community climate system model. *International Journal for High Performance Computing Applications*, 19(3), 309–327. <https://doi.org/10.1177/1094342005056117>
- Craig, A. P., Vertenstein, M., & Jacob, R. (2012). A new flexible coupler for earth system modeling developed for CCSM4 and CESM1. *International Journal for High Performance Computing Applications*, 26(1), 31–42. <https://doi.org/10.1177/1094342011428141>
- Cubasch, U., and R. D.Cess (1990). Processes and modeling. *Climate Change: The IPCC Scientific Assessment*, edited by J. T. Houghton et al., chap. 3, (pp. 69–72). Cambridge Univ. Press, Cambridge, U. K., and New York.

Doescher, E., H. de Campos Velho & F. M. Ramos (2002). Different grid strategies in fluid dynamics. In *Advances in Fluid Mechanics IV*, edited by M. Rahman et al., (pp. 587-596). Wit Press, Dalhousie University, Canada, Ghent University, Belgium Wessex Institute of Technology, Southampton, U. K.  
Retrieved from <https://www.witpress.com/Secure/elibrary/papers/AFM02/AFM02054FU.pdf>

Eyring, V., S. Bony, G. A. Meehl, C. A. Senior, B. Stevens, R. J. Stouffer, et al. (2016). Overview of the Coupled Model Intercomparison Project phase 6 (CMIP6) experimental design and organization. *Geoscientific Model Development*, 9(5), 1937-1958.  
<https://doi.org/10.5194/gmd-9-1937-2016>

Flato, G., J. Marotzke, B. Abiodun, P. Braconnot, S.C. Chou, W. Collins, et al. (2013). Evaluation of climate models. In *Climate Change 2013: The Physical Science Basis. Contribution of Working Group I to the Fifth Assessment Report of the Intergovernmental Panel on Climate Change*, edited by T. Stocker et al., chap. 9, (pp. 741–866). Cambridge Univ. Press, Cambridge, U. K., and New York.

Friedrich, T., A. Timmermann, M. Tigchelaar, O. E. Timm, and A. Ganopolski (2016). Nonlinear climate sensitivity and its implications for future greenhouse warming. *Science Advances*, 2(11), e1501923. <https://doi.org/10.1126/sciadv.1501923>

Fu, Q., and K. N. Liou (1992). On the correlated K-distribution method for radiative-transfer in nonhomogeneous atmospheres. *Journal of the Atmospheric Sciences*, 49(22), 2139-2156.  
[https://doi.org/10.1175/1520-0469\(1992\)049<2139:Otcdmf>2.0.Co;2](https://doi.org/10.1175/1520-0469(1992)049<2139:Otcdmf>2.0.Co;2)

Gao, J. Q., Z. H. Xie, A. W. Wang, S. Liu, Y. J. Zeng, B. Liu, et al. (2019). A new frozen soil parameterization including frost and thaw fronts in the community land model. *Journal of Advances in Modeling Earth Systems*, 11(3), 659-679.  
<https://doi.org/10.1029/2018ms001399>

Gao, J. Q., Z. H. Xie, A. W. Wang, and Z. D. Luo (2016). Numerical simulation based on two-directional freeze and thaw algorithm for thermal diffusion model. *Appl Math Mech-Engl*, 37(11), 1467-1478. <https://doi.org/10.1007/s10483-016-2106-8>

Gettelman, A., L. Lin, B. Medeiros, and J. Olson (2016). Climate feedback variance and the interaction of aerosol forcing and feedbacks. *Journal of Climate*, 29(18), 6659-6675.  
<https://doi.org/10.1175/Jcli-D-16-0151.1>

Gregory, J. M., W. J. Ingram, M. A. Palmer, G. S. Jones, P. A. Stott, R. B. Thorpe, et al. (2004). A new method for diagnosing radiative forcing and climate sensitivity. *Geophysical Research Letters*, 31, L03205. <https://doi.org/10.1029/2003GL018747>

Hansen, J., M. Sato, R. Ruedy, L. Nazarenko, A. Lacis, G. A. Schmidt, et al. (2005). Efficacy of climate forcings. *Journal of Geophysical Research: Atmospheres*, 110, D18104.  
<https://doi.org/10.1029/2005JD005776>



He, J., M. Winton, G.A. Vecchi, L. Jia and M. Rugenstein (2017). Transient climate sensitivity depends on base climate ocean circulation. *Journal of Climate*, 30(4), 1493-1504. <https://doi.org/10.1175/JCLI-D-16-0581.1>

Huang, Y., A. Protat, S. T. Siems, and M. J. Manton (2015). A-Train observations of maritime mid-latitude storm-track cloud systems: Comparing the Southern Ocean against the North Atlantic. *J. Clim.*, 28, 1920–1939. <https://doi.org/10.1175/JCLI-D-14-00169.1>

Hu, Y., S. Rodier, K. man Xu, W. Sun, J. Huang, B. Lin, P. Zhai, and D. Josset (2010). Occurrence, liquid water content, and fraction of supercooled water clouds from combined CALIOP/IIR/MODIS measurements. *J. Geophys. Res.*, 115, D00H34. <https://doi.org/10.1029/2009JD012384>

Jonko, A. K., K. M. Shell, B. M. Sanderson, and G. Danabasoglu (2012). Climate feedbacks in CCSM3 under changing CO2 forcing. Part I: Adapting the linear radiative kernel technique to feedback calculations for a broad range of forcings. *Journal of Climate*, 25(15), 5260-5272. <https://doi.org/10.1175/Jcli-D-11-00524.1>

Knutti, R., and G. Hegerl (2008). The equilibrium sensitivity of the earth's temperature to radiation changes. *Nature Geosci*, 1, 735-743. <https://doi.org/10.1038/ngeo337>

Levermann, A., J. Mignot, S. Nawrath, and S. Rahmstorf (2007). The Role of Northern Sea Ice Cover for the Weakening of the Thermohaline Circulation under Global Warming. *J. Climate*, 20, 4160–4171. <https://doi.org/10.1175/JCLI4232.1>

Li, L. J., B. Wang, L. Dong, L. Liu, S. Shen, N. Hu, et al. (2013a). Evaluation of Grid-point Atmospheric Model of IAP LASG Version 2 (GAMIL2). *Advances in Atmospheric Sciences*, 30(3), 855–867. <https://doi.org/10.1007/s00376-013-2157-5>

Li, L., B. Wang, and G. J. Zhang. (2014). The Role of Nonconvective Condensation Processes in Response of Surface Shortwave Cloud Radiative Forcing to El Niño Warming. *J. Climate*, 27, 6721–6736. <https://doi.org/10.1175/JCLI-D-13-00632.1>

Li, L., B. Wang, and G. J. Zhang. (2015). The Role of Moist Processes in Shortwave Radiative Feedback during ENSO in the CMIP5 Models. *J. Climate*, 28, 9892–9908. <https://doi.org/10.1175/JCLI-D-15-0276.1>

Li, L. J., L. Dong, J. B. Xie, Y. L. Tang, F. Xie, Z. Guo, et al. (2020b). The Grid-point Atmospheric Model of the IAP LASG version 3 (GAMIL3): Model Description and Evaluation, *Journal of Geophysical Research-Atmosphere*. <https://doi.org/10.1029/2020JD032574>

Li, L. J., P. F. Lin, Y. Q. Yu, B. Wang, T. J. Zhou, L. Liu, et al. (2013b). The Flexible Global Ocean-Atmosphere-Land System Model, Grid-point Version 2: FGOALS-g2. *Advances in Atmospheric Sciences*, 30(3), 543-560.

<https://doi.org/10.1007/s00376-012-2140-6>

Li, L. J., Y. Q. Yu, Y. L. Tang, P. F. Lin, J. B. Xie, M. R. Song, et al. (2020a). The Flexible Global Ocean-Atmosphere-Land System Model Grid-Point Version 3 (FGOALS-g3): Description and Evaluation. *Journal of Advances in Modeling Earth Systems*, 12, e2019MS002012. <https://doi.org/10.1029/2019MS002012>

Li, X. L., Y. Q. Yu, and H. L. Liu (2017). Sensitivity of Atlantic meridional overturning circulation to the dynamical framework in an ocean general circulation model. *J Meteorol Res*, 31, 490–501. <https://doi.org/10.1007/s13351-017-6109-3>

Lin, P. F., Z. P. Yu, H. L. Liu, Y. Q. Yu, Y. W. Li, J. R. Jiang, et al. (2020). LICOM Model Datasets for the CMIP6 Ocean Model Intercomparison Project. *Adv. Atmos. Sci.* 37, 239–249. <https://doi.org/10.1007/s00376-019-9208-5>

Liu, H. L., P. F. Lin, and Y. Q. Yu, (2012). The baseline evaluation of LASG/IAP Climate System Ocean Model (LICOM) Version 2.0. *Acta Meteorologica Sinica*, 26(3), 318-329. <https://doi.org/10.1007/s13351-012-0305-y>

Liu, J. P. (2010). Sensitivity of sea ice and ocean simulations to sea ice salinity in a coupled global climate model. *Sci China Earth Sci*, 53(6), 911-918. <https://doi.org/10.1007/s11430-010-0051-x>

Liu, S., Z. H. Xie, Y. J. Zeng, B. Liu, R. C. Li, Y. Wang, et al. (2019). Effects of anthropogenic nitrogen discharge on dissolved inorganic nitrogen transport in global rivers. *Global Change Biol*, 25(4), 1493-1513. <https://doi.org/10.1111/gcb.14570>

Mach, K.J., S. Planton and C. von Stechow (2014). Glossary. In *Climate Change 2014: Synthesis Report. Contribution of Working Groups I, II and III to the Fifth Assessment Report of the Intergovernmental Panel on Climate Change*, edited by R.K. Pachauri et al., Annex II, (pp. 117-130). Geneva, Switzerland.

McGregor, J.L. (2015). Recent developments in variable-resolution global climate modelling. *Climatic Change*, 129, 369–380. <https://doi.org/10.1007/s10584-013-0866-5>

Medhaug, I., and T. Furevik, (2011). North Atlantic 20th century multidecadal variability in coupled climate models: Sea surface temperature and ocean overturning circulation. *Ocean Sci.*, 7, 389–404. <https://doi.org/10.5194/os-7-389-2011>

Oleson, K., Dai, Y., Bonan, G. B., Bosilovich, M., Dickinson, R., Dirmeyer, P., et al. (2004). Technical Description of the Community Land Model (CLM) (No. NCAR/TN-461+STR). University Corporation for Atmospheric Research. <https://doi.org/10.5065/D6N877R0>

Oleson, K., Lawrence, D. M., Bonan, G. B., Drewniak, B., Huang, M., Koven, C. D., et al. (2013). Technical description of version 4.5 of the Community Land Model (CLM) (No. NCAR/TN-503+STR). <https://doi.org/10.5065/D6RR1W7M>

Pendergrass, Angeline & National Center for Atmospheric Research Staff (Eds). (2018). *The Climate Data Guide: Radiative kernels from climate models*. The CAM5 kernels retrieved from <https://climatedataguide.ucar.edu/climate-data/radiative-kernels-climate-models>. <https://doi.org/10.5065/D6F47MT6>

Randall, D.A., R.A. Wood, S. Bony, R. Colman, T. Fichet, J. Fyfe, et al. (2007). Climate models and their evaluation. In *Climate Change 2007: The Physical Science Basis. Contribution of Working Group I to the Fourth Assessment Report of the Intergovernmental Panel on Climate Change*, edited by S. Solomon et al., chap. 8, (pp. 589–662). Cambridge Univ. Press, Cambridge, U. K., and New York.

Schlund, M., A. Lauer, P. Gentile, S. C. Sherwood, V. Eyring (2020). Emergent constraints on Equilibrium Climate Sensitivity in CMIP5: do they hold for CMIP6?. *Earth System Dynamics*. <https://doi.org/10.5194/esd-2020-49>

Senior, C. A., and J. F. B. Mitchell (2000). The time-dependence of climate sensitivity. *Geophysical Research Letters*, 27(17), 2685-2688. <https://doi.org/10.1029/2000gl011373>

Shell, K. M., J. T. Kiehl, and C. A. Shields (2008). Using the radiative kernel technique to calculate climate feedbacks in NCAR's community atmospheric model. *Journal of Climate*, 21(10), 2269-2282. <https://doi.org/10.1175/2007jcli2044.1>

Shine, K. P., J. Cook, E. J. Highwood, and M. M. Joshi (2003). An alternative to radiative forcing for estimating the relative importance of climate change mechanisms. *Geophysical Research Letters*, 30(20), 2047. <https://doi.org/10.1029/2003GL018141>

Silvers, L.G., D.J. Paynter, and M. Zhao (2018). The diversity of cloud responses to twentieth century sea surface temperatures. *Geophysical Research Letters*, 45(1), 391-400. <https://doi.org/10.1002/2017GL075583>

Soden, B. J., A. J. Broccoli, and R. S. Hemler (2004). On the use of cloud forcing to estimate cloud feedback. *Journal of Climate*, 17(19), 3661-3665. [https://doi.org/10.1175/1520-0442\(2004\)017<3661:Otuocf>2.0.Co;2](https://doi.org/10.1175/1520-0442(2004)017<3661:Otuocf>2.0.Co;2)

Soden, B. J., and I. M. Held (2006). An assessment of climate feedbacks in coupled ocean-atmosphere models. *Journal of Climate*, 19(23), 6263-6263. <https://doi.org/10.1175/Jcli9028.1>

Soden, B. J., I. M. Held, R. Colman, K. M. Shell, J. T. Kiehl, and C. A. Shields (2008). Quantifying climate feedbacks using radiative kernels. *Journal of Climate*, 21(14), 3504-3520. <https://doi.org/10.1175/2007jcli2110.1>

- Taylor, K. E., R. J. Stouffer, and G. A. Meehl, (2012). An overview of CMIP5 and the experiment design. *Bulletin of the American Meteorological Society*, 93, 485–498. <https://doi.org/10.1175/BAMS-D-11-00094.1>
- Tian, B. J. (2015). Spread of model climate sensitivity linked to double-intertropical convergence zone bias. *Geophysical Research Letters*, 42(10), 4133-4141. <https://doi.org/10.1002/2015gl064119>
- Turner, D. D., A. M. Vogelmann, R. T. Austin, J. C. Barnard, K. Cady-Pereira, J. C. Chiu, et al. (2007). Thin liquid water clouds: Their importance and our challenge. *Bull. Am. Meteorol. Soc.*, 88(2), 177–190. <https://doi.org/10.1175/BAMS-88-2-177>
- Vial, J., S. Bony, B. Stevens, and R. Vogel (2017). Mechanisms and model diversity of trade-wind shallow cumulus cloud feedbacks: A review. *Surveys in Geophysics*, 38(6), 1331-1353. <https://doi.org/10.1007/s10712-017-9418-2>.
- Vial, J., J. L. Dufresne, and S. Bony (2013). On the interpretation of inter-model spread in CMIP5 climate sensitivity estimates. *Climate Dynamics*, 41(11-12), 3339-3362. <https://doi.org/10.1007/s00382-013-1725-9>
- Weijer, W, W. Cheng, O. A. Garuba, A. Hu, and B. T. Nadiga (2020). CMIP6 Models Predict Significant 21st Century Decline of the Atlantic Meridional Overturning Circulation. *Geophysical Research Letters*, 47, e2019GL086075. <https://doi.org/10.1029/2019GL086075>
- Wetherald, R., and S. Manabe (1988). Cloud feedback processes in a general circulation model. *Journal of The Atmospheric Sciences*, 45, 1397-1416. [https://doi.org/10.1175/1520-0469\(1988\)045<1397:CFPIAG>2.0.CO;2](https://doi.org/10.1175/1520-0469(1988)045<1397:CFPIAG>2.0.CO;2)
- Winton, M. (2006). Surface Albedo Feedback Estimates for the AR4 Climate Models. *Journal of Climate*, 19, 359–365. <https://doi.org/10.1175/JCLI3624.1>
- Wyser, K., van Noije, T., Yang, S., von Hardenberg, J., O'Donnell, D., and Döscher, R. (2020). On the increased climate sensitivity in the EC-Earth model from CMIP5 to CMIP6, *Geosci. Model Dev.*, 13, 3465–3474, <https://doi.org/10.5194/gmd-13-3465-2020>
- Xie, Z. H., Liu, S., Zeng, Y. J., Gao, J. Q., Qin, P. H., Jia, B. H., et al. (2018). A high-resolution land model with groundwater lateral flow, water use, and soil freeze-thaw front dynamics and its Application in an endorheic basin. *Journal of Geophysical Research: Atmospheres*, 123(14), 7204-7222. <https://doi.org/10.1029/2018jd028369>
- Xie, Z. H., Z. H. Di, Z. D. Luo, & Q. Ma (2012). A quasi-three-dimensional variably saturated groundwater flow model for climate modeling. *Journal of Hydrometeorology*, 13(1), 27–46. <http://doi.org/10.1175/JHM-D-10-05019.1>

- Yu, Y. Q., S. L. Tang, H. L. Liu, P. F. Lin, X. L. Li (2018). Development and evaluation of the dynamic framework of an ocean general circulation model with arbitrary orthogonal curvilinear coordinate. *Chinese Journal of Atmospheric Sciences*, 42(4), 877-889.  
<https://doi.org/10.3878/j.issn.1006-9895.1805.17284>
- Zeebe, R. E. (2011), Where are you heading earth?. *Nature Geoscience*, 4(7), 416-417.  
<https://doi.org/10.1038/ngeo1196>
- Zelinka, M. D., S. A. Klein, and D. L. Hartmann (2012). Computing and partitioning cloud feedbacks using cloud property histograms. Part II: Attribution to changes in cloud amount, altitude, and optical depth. *Journal of Climate*, 25(11), 3736-3754.  
<https://doi.org/10.1175/Jcli-D-11-00249.1>
- Zelinka, M. D., T. A. Myers, D. T. McCoy, S. Po-Chedley, P. M. Caldwell, P. Ceppi, et al. (2020). Causes of higher climate sensitivity in CMIP6 models. *Geophysical Research Letters*, 47, e2019GL085782. <https://doi.org/10.1029/2019gl085782>
- Zeng, Y. J., Z. H. Xie, S. Liu, J. B. Xie, B. H. Jia, P. H. Qin, et al. (2018). Global land surface modeling including lateral groundwater flow. *Journal of Advances in Modeling Earth Systems*, 10. <https://doi.org/10.1029/2018MS001304>
- Zeng, Y. J., Z. H. Xie, Y. Yu, S. Liu, L. Y. Wang, J. Zou, et al. (2016). Effects of anthropogenic water regulation and groundwater lateral flow on land processes. *Journal of Advances in Modeling Earth Systems*, 8, 1106-1131
- Zhang, M. H., J. J. Hack, J. T. Kiehl, and R. D. Cess (1994). Diagnostic study of climate feedback processes in atmospheric general circulation models. *Journal of Geophysical Research: Atmospheres*, 99(D3), 5525-5537. <https://doi.org/10.1029/93jd03523>
- Zhao, M., J-C Golaz, I.M. Held, V. Ramaswamy, S.-J. Lin, Y. Ming, et al. (2016). Uncertainty in model climate sensitivity traced to representations of cumulus precipitation microphysics. *Journal of Climate*, 29(2), 543-560.  
<https://doi.org/10.1175/JCLI-D-15-0191.1>
- Zhou, T. J., L. W. Zou, X. L. Chen (2019) Commentary on the Coupled Model Intercomparison Project phase 6 (CMIP6) [J]. *Climate Change Research*, 15 (5): 445-456.  
<https://doi.org/10.12006/j.issn.1673-1719.2019.193>
- Zou J, Z. H. Xie, Y. Yu, C. S. Zhan, Q. Sun (2014). Climatic responses to anthropogenic groundwater exploitation: a case study of the Haihe River basin, northern China. *Climate Dynamics*, 2014, 42, 2125-2145.  
<https://doi.org/10.1007/s00382-013-1995-2>

**Table 1.** Vertically-integrated (up to the tropopause) global and decadal mean values of feedback parameters ( $\lambda_T$ ,  $\lambda_{\text{Planck}}$ ,  $\lambda_{\text{LR}}$ ,  $\lambda_{\text{WV}}$ ,  $\lambda_\alpha$ , and  $\lambda_c$ ) given in  $\text{W m}^2 \text{K}^{-1}$ , and their sum ( $\lambda_{\text{sum}}$ ) estimated using the CAM5 radiative kernels and CRE under all-sky conditions. The total feedbacks ( $\lambda_{\text{tot}}$ ) were calculated using the method of Gregory et al. (2004). ‘Res’ indicates the difference between  $\lambda_{\text{tot}}$  and  $\lambda_{\text{sum}}$ .

version	stage	$\lambda_T$	$\lambda_{\text{Planck}}$	$\lambda_{\text{LR}}$	$\lambda_{\text{WV}}$	$\lambda_{\text{WV+LR}}$	$\lambda_{\text{Albedo}}$	$\lambda_c$	$\lambda_{\text{sum}}$	$\lambda_{\text{tot}}$	Res
FGOALS -g3	All	-3.5986	-3.1855	-0.4167	2.3278	1.9112	0.5364	-0.3978	-1.1321	-1.3088	-0.1767
	Fast	-3.7650	-3.1750	-0.5940	2.4429	1.8489	0.5380	-0.5423	-1.3263	-1.5000	-0.1737
	Slow	-3.2332	-3.1442	-0.0927	2.3241	2.2314	0.5204	-0.1811	-0.5698	-1.0400	-0.4702
FGOALS -g2	All	-3.4004	-3.1440	-0.2629	2.0494	1.7865	0.6218	-0.0218	-0.7511	-0.8692	-0.1181
	Fast	-3.7775	-3.2110	-0.5729	2.3402	1.7673	0.3764	-0.2902	-1.3511	-1.3700	-0.0189
	Slow	-3.1705	-3.0966	-0.0802	2.1944	2.1142	0.7478	0.0236	-0.2048	-0.6500	-0.4452

**Figure 1.** The residual term of the three cloud feedback calculation methods: the CAM5 radiative kernel method (group 1), the wholly simplified method ( $\lambda_{cloud\_corr} = 0$ ) (group 2), and the simplified method ( $\lambda_{cloud\_corr} \neq 0$ ) (group 3).

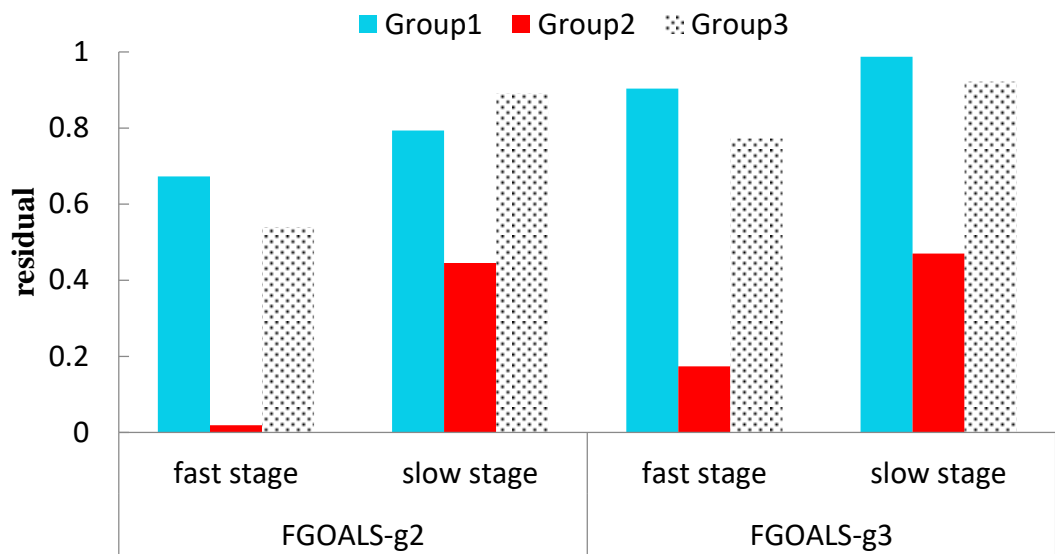


**Figure 2.** TOA net radiation against global mean SAT change in the abrupt4×CO<sub>2</sub> scenario relative to the piControl run for (a) FGOALS-g3 and (b) FGOALS-g2. The black lines show the fast-response stage (the first 20 years) and the slow-response stage (the last 130 years). The red lines show all 150 years.

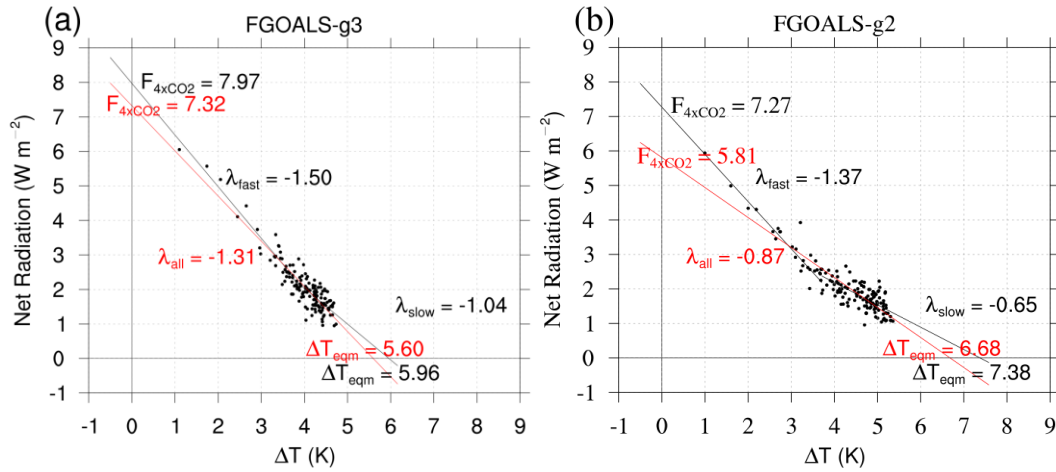




**Figure 3.** (a) The SAT anomaly change in the abrupt4×CO<sub>2</sub> experiment relative to the piControl run (solid line), and the SAT base state in the piControl simulation (dashed line) for FGOALS-g2 (blue) and FGOALS-g3 (red). (b) The SIA anomaly change in the Northern Hemisphere (solid line) and Southern Hemisphere (dashed line) in the abrupt4×CO<sub>2</sub> experiment relative to the piControl run, and the SIA base state in the Northern Hemisphere (dots) and Southern Hemisphere (plus signs) in the piControl simulation for FGOALS-g2 (blue) and FGOALS-g3 (red).

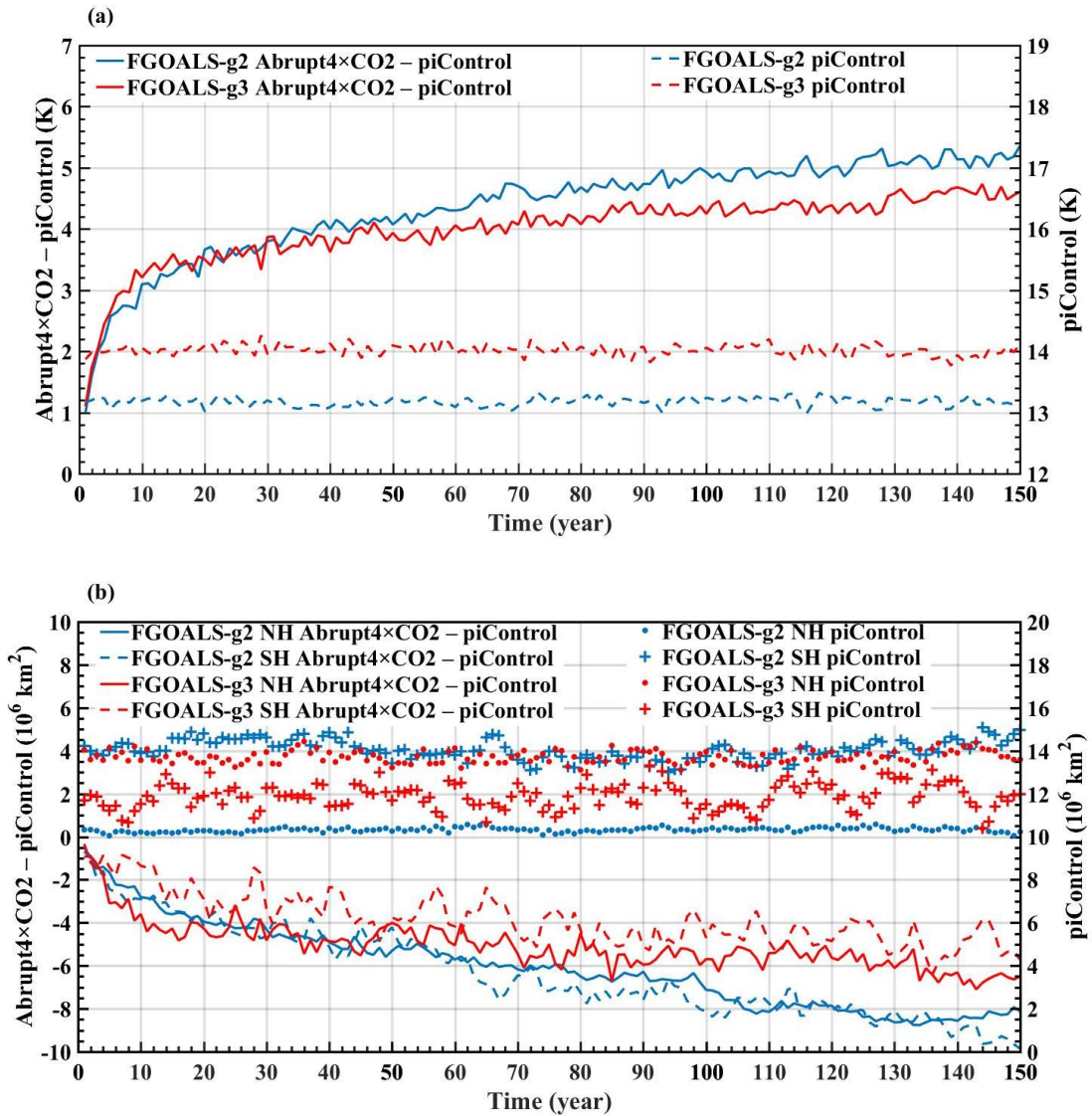


**Figure 4.** Difference of climate feedback parameters between FGOALS-g3 and FGOALS-g2, including the total feedback parameter  $\lambda_{\text{tot}}$  (calculated using the all-sky net radiation against the global mean SAT change in the abrupt4 $\times$ CO2 scenario relative to the piControl run), its components ( $\lambda_{\text{T}}$ ,  $\lambda_{\text{Planck}}$ ,  $\lambda_{\text{LR}}$ ,  $\lambda_{\text{WV}}$ ,  $\lambda_{\alpha}$ , and  $\lambda_{\text{c}}$ ), and the sum of all components ( $\lambda_{\text{sum}}$ ). The residual, Res, is equal to  $\lambda_{\text{tot}} - \lambda_{\text{sum}}$ .

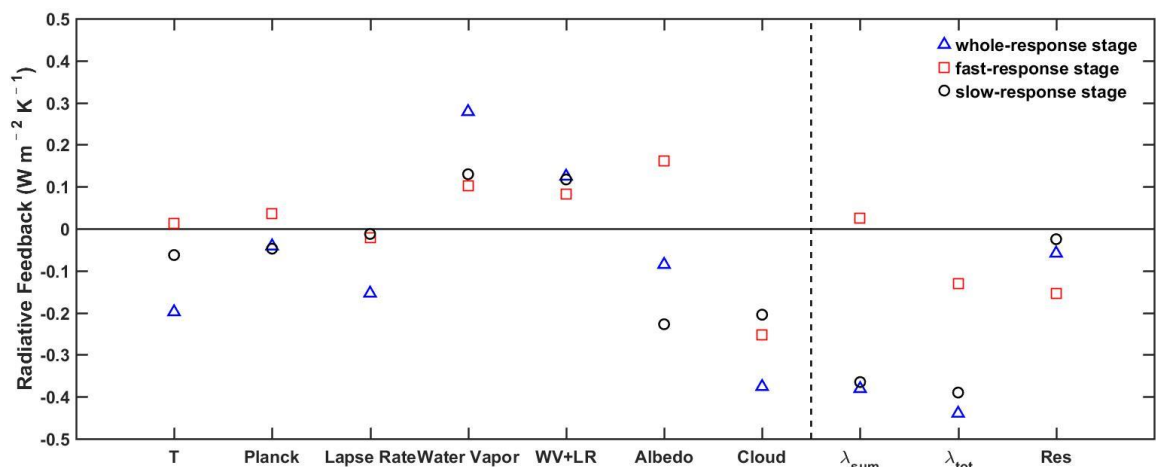


**Figure 5.** Surface albedo feedback (color fill), SAT (contour line), and SIA (shadow fill) in the versions of the two model around the Arctic. (a), (b) The surface albedo feedback in the fast-response stage, and the change of SAT and SIA from the 10<sup>th</sup> to the 20<sup>th</sup> year in the abrupt4×CO<sub>2</sub> experiment relative to the piControl run. (c), (d) The surface albedo feedback in the slow-response stage, and the change of SAT and SIA from the 140<sup>th</sup> to the 150<sup>th</sup> year in the abrupt4×CO<sub>2</sub> experiment relative to the piControl run. (a), (c) FGOALS-g3, (b), (d) FGOALS-g2.

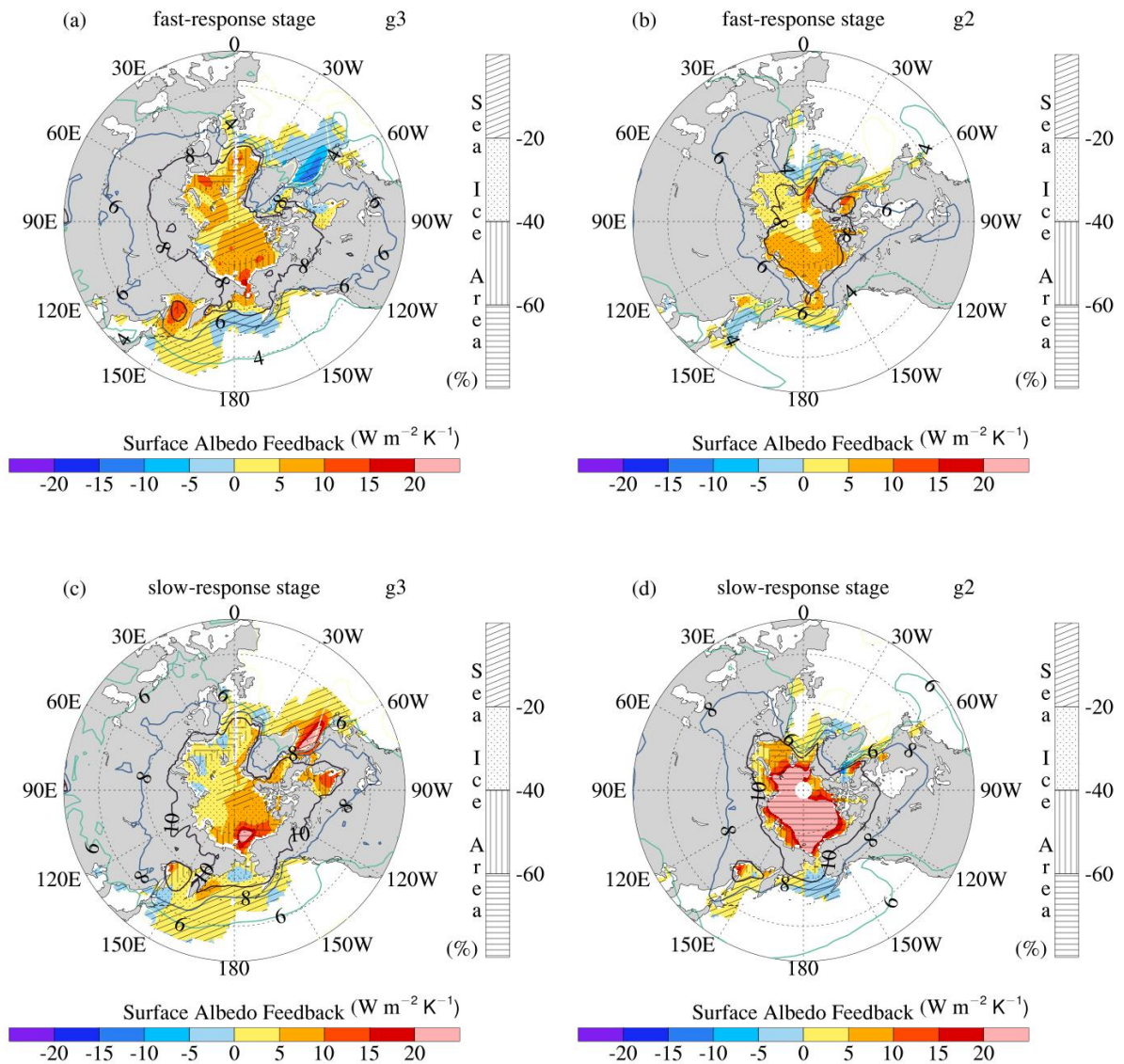


**Figure 6.** The AMOC index anomaly change in the abrupt4×CO<sub>2</sub> experiment relative to the piControl run (solid line) and the AMOC index base state in the piControl run (dashed line) for FGOALS-g2 (blue) and FGOALS-g3 (red). The AMOC index is defined as the maximum of the meridional overturning stream function between 15°N and 65°N below 500 m in depth.

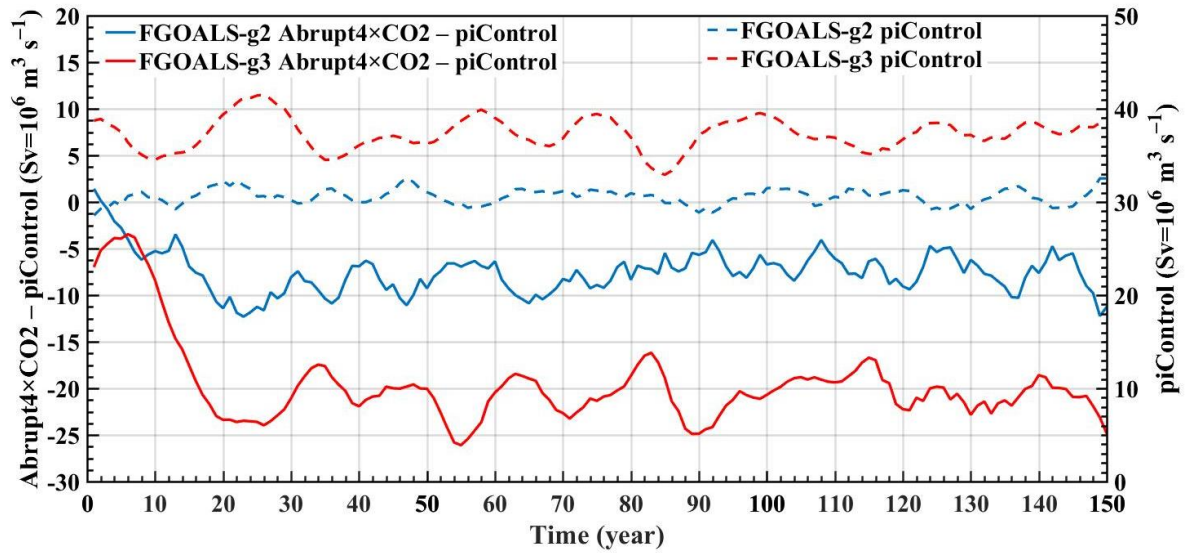


**Figure 7.** Anomaly change in the abrupt4×CO<sub>2</sub> experiment relative to the piControl run (solid line), and the base state in the piControl run (dashed line) for FGOALS-g2 (blue) and FGOALS-g3 (red). (a) Total cloud area fraction (CAF), (b) liquid water path (LWP), and (c) ice water path (IWP).

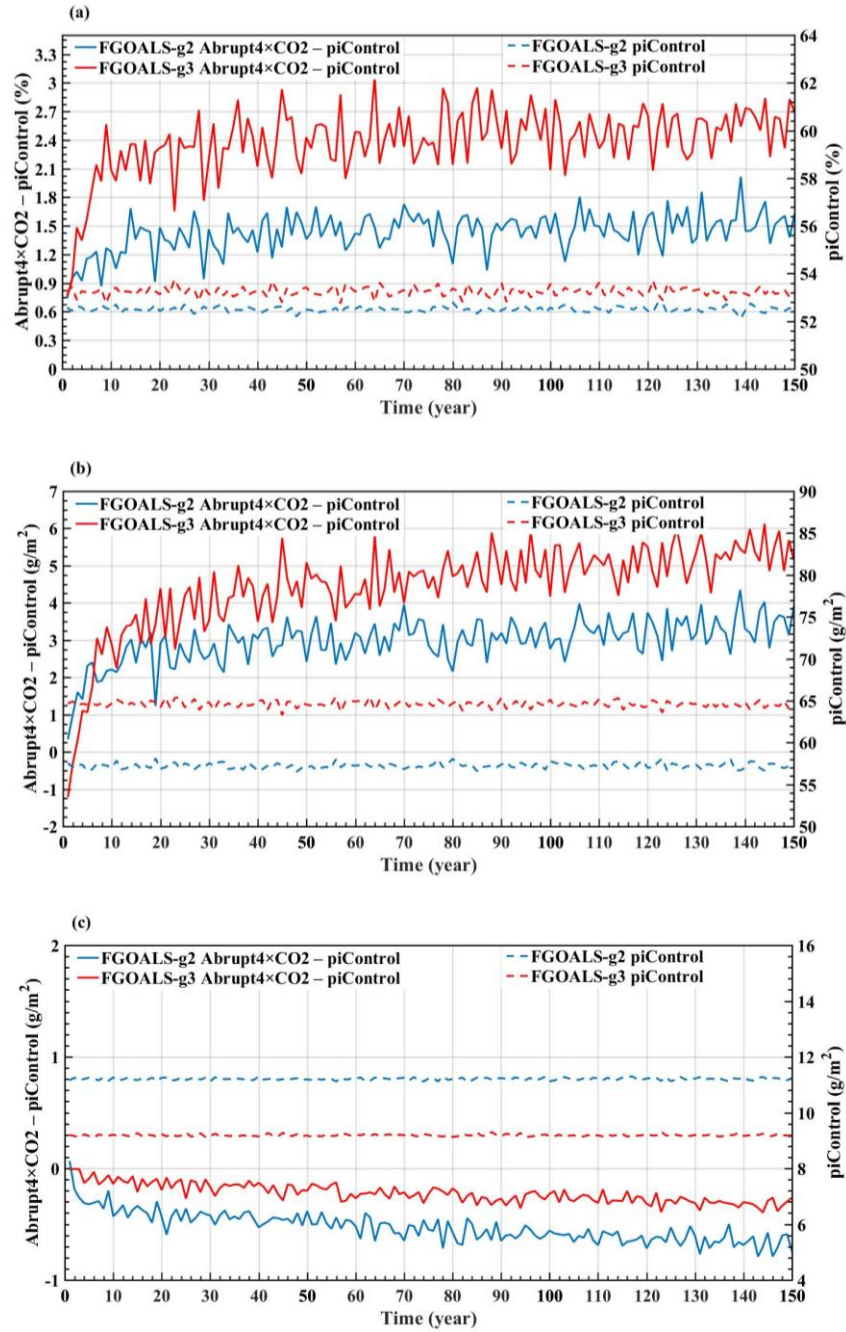




**Figure 8.** The difference in the distribution of (a) cloud feedback, (b) water vapor feedback, and (c) cloud SW feedback between FGOALS-g3 and FGOALS-g2.

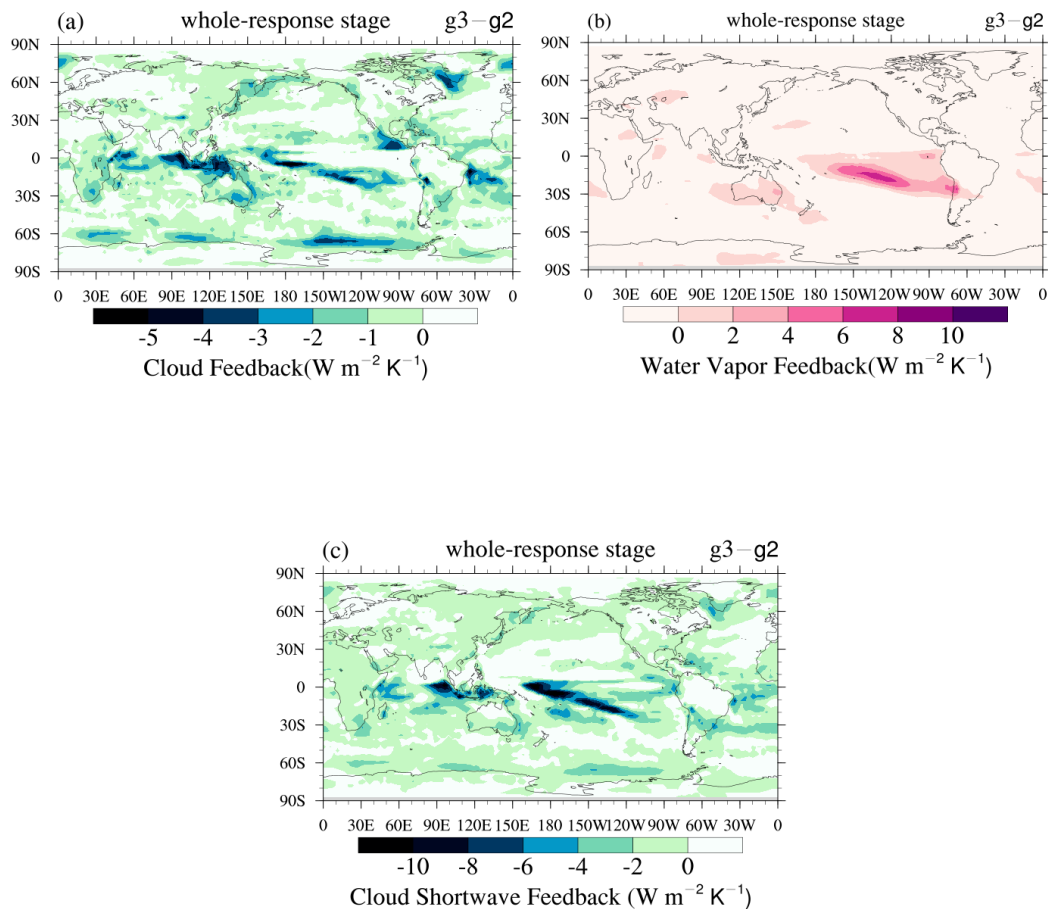


**Figure 9.** The CAF profile anomaly in the abrupt4×CO2 experiment relative to the piControl run for (a) FGOALS-g3 and (b) FGOALS-g2.

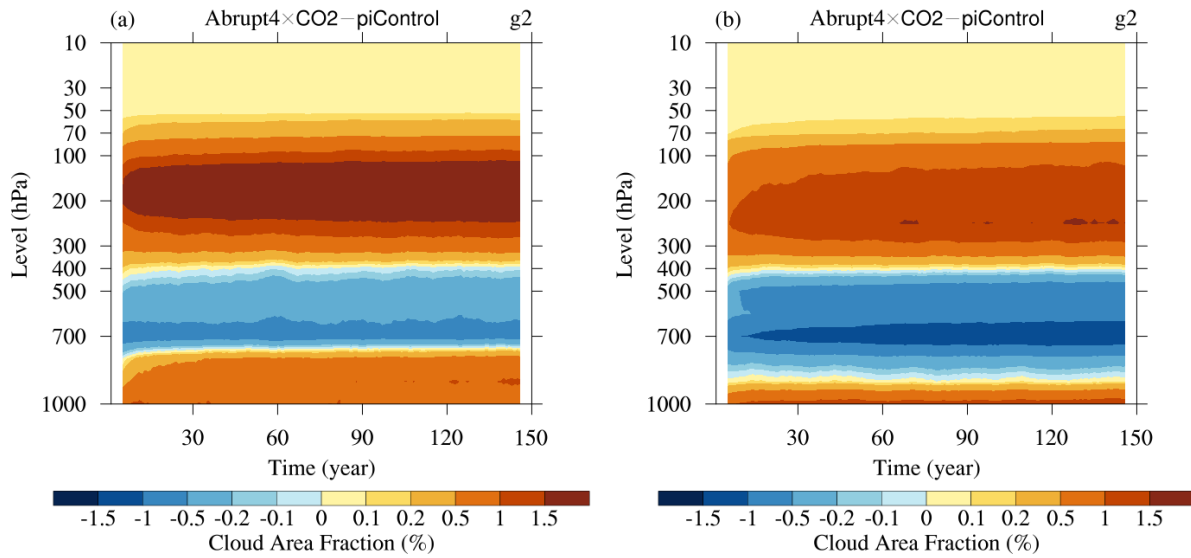


**Figure 10.** The LW and SW residual term in the abrupt4×CO<sub>2</sub> scenario relative to the piControl run. (a) The LW residual term of FGOALS-g3. (b) The LW residual term of FGOALS-g2. (c) The SW residual term of FGOALS-g3.(d) The SW residual term of FGOALS-g2.

